Materials Advances

ROYAL SOCIETY OF CHEMISTRY

PAPER

View Article Online
View Journal

Cite this: DOI: 10.1039/d6ma00411c

Low-temperature molten salt shielded synthesis of semiconducting Mn-doped β-$FeSi_2$ under ambient air conditions

Hemalatha M. Sivaprakasam, Rajasekar Parasuraman * and Arun Anand Prabu *

Received 24th March 2026,
Accepted 30th May 2026

DOI: 10.1039/d6ma00411c

rsc.li/materials-advances

β-$FeSi_2$ has emerged as a promising, low-cost, and eco-friendly semiconducting material with strong potential for energy-related applications. However, conventional synthesis methods typically require high temperatures and controlled environments such as vacuum or inert atmospheres, which increase manufacturing costs and limit scalability. In this work, we report an economical and scalable molten salt shielded synthesis method for producing semiconducting Mn-doped β-$FeSi_2$ with minor Si and oxide secondary phases, which was confirmed by X-ray diffraction. Morphology and nominal elemental composition were examined using field-emission scanning electron microscopy and energy-dispersive X-ray spectroscopy. Furthermore, X-ray photoelectron spectroscopy was employed to investigate the surface chemical composition of the synthesized material. Temperature-dependent resistivity measurements of the as-synthesized pellet confirm its semiconducting behavior. Overall, the results demonstrate that MS3 is a simple, scalable, and cost-effective approach for preparing semiconducting β-$FeSi_2$ in powder form. The obtained powder can be utilized for fabricating composite or flexible devices for energy-related applications.

1 Introduction

Semiconducting materials synthesized in nano/microscale powder form can be incorporated into polymer matrices to form functional composite materials. These composite materials are used in the fabrication of flexible thermoelectric modules, flexible solar cells and flexible electronics. The powder–polymer approach enables low-temperature processing, mechanical flexibility, and scalable solution-based manufacturing techniques, making it attractive for next-generation wearable and large-area energy devices. Semiconducting transition metal silicides (TMs) show excellent electrical conductivity, stability, and strong resistance to corrosion and oxidation. Among the various transition metal silicides, β-$FeSi_2$ garnered widespread interest because of its stability at higher temperature and in harsh chemical environments. β-$FeSi_2$ is a semiconducting material with a band gap of 0.8 eV and crystallizes in the orthorhombic *Cmca* space group. It consists of elements that are earth abundant, low cost, non-toxic and environmentally friendly in nature. Intrinsic β-$FeSi_2$ can be made into either n-type by Co, Ni (Fe site) doping/P doping (Si site) or p-type by doping it with Mn, Cr (Fe site)/Al (Si site).[1,2]

From the literature, intrinsic β-$FeSi_2$ shows room-temperature resistivity values in the range of 10^1–10^3 Ω cm with carrier concentrations of ~10^{14}–10^{16} cm^{-3} and mobility values of 10–200 $cm^2\ V^{-1}\ s^{-1}$. This reflects its low intrinsic carrier density and semiconducting nature.[3,4] Upon n-type β-$FeSi_2$ doping, the carrier concentration increases significantly to about 10^{17}–10^{18} cm^{-3}. The mobility falls in the range of 5–100 $cm^2\ V^{-1}\ s^{-1}$, due to doping, and the resistivity decreases to the range of 1–10^{-3} Ω cm. Similarly, p-type β-$FeSi_2$ exhibits a resistivity of 10–10^{-2} Ω cm with carrier concentrations of approximately 10^{17}–10^{19} cm^{-3} and mobilities in the range of 2–50 $cm^2\ V^{-1}\ s^{-1}$, depending on dopant type and concentration.[5–9] Recent studies have shown that improved thermoelectric performance in β-$FeSi_2$ is achieved through densification, microstructural optimization and doping, which enhance grain connectivity and reduce interfacial resistance.[10–13] The excellent high-temperature stability, environmental friendliness, tuneable carrier type and carrier concentration make β-$FeSi_2$ a potential material for photovoltaic, thermoelectric, and optoelectronic applications.

The Fe–Si binary phase diagram exhibits complex interactions between metallic phases (Fe, α-Fe_2Si_5, and ε-FeSi) and semiconducting phases (β-$FeSi_2$ and Si). β-$FeSi_2$ does not form directly from the melt. During the initial solidification of arc-melted Fe and Si, α-Fe_2Si_5 and ε-FeSi are formed, which are subsequently heat-treated (at 873–1073 K for 12–100 h) to produce β-$FeSi_2$. However, this peritectoid reaction between the metallic α and ε phases proceeds very slowly and shows sluggish kinetics (α-Fe_2Si_5 + ε-FeSi → β-$FeSi_2$).[14,15] As an alternative approach, arc melting

Department of Chemistry, School of Advanced Sciences, Vellore Institute of Technology, Vellore, Tamil Nadu, 632 014, India.
E-mail: rajasekar.mgac@gmail.com, anandprabu@vit.ac.in

with excess Si leads to the formation of α-Fe_2Si_5 along with residual silicon. Subsequent heat treatment facilitates the eutectoid reaction below 1138 K (α-Fe_2Si_5 → β-$FeSi_2$ + Si). This eutectoid-based route significantly reduces the reaction time and results in the formation of a Si-dispersed β-$FeSi_2$ composite.[16–20]

As another approach, a direct solid-state reaction between Fe and Si is carried out by ball milling or reactive sintering below 973 K to achieve the formation of β-$FeSi_2$. Ur *et al.* synthesized Co-doped n-type $FeSi_2$ using mechanical alloying followed by heat treatment at ∼1073 K, which promotes the formation of β-$FeSi_2$ with improved electrical transport properties. These studies demonstrate that mechanical alloying enables controlled phase formation and improved microstructural characteristics in $FeSi_2$-based thermoelectric materials.[21] Yamada *et al.* reported the low-temperature synthesis of β-$FeSi_2$ powder using a sodium melt method, where sodium melt was used as the reaction medium and elemental Fe and Si were reacted in a ratio of 1 : 2.25–2.5 under an argon atmosphere.[22,23] The reported reaction time ranged from 1.5 to 24 h at temperatures between 673 and 1073 K. This sodium flux method has also been used to synthesize other silicides such as $MnSi_{1.7}$, $CrSi_2$, and CoSi. The conventional sodium flux method used for silicide synthesis requires inert or vacuum conditions due to the high reactivity of sodium toward moisture and oxygen. Although semiconducting β-$FeSi_2$ can be synthesized by methods such as arc melting, induction melting, ball milling, spark plasma sintering (SPS), hot pressing, mechanical alloying, and chemical synthesis in both bulk and thin-film forms, most of these approaches require an argon atmosphere or vacuum and prolonged heat treatment to stabilize the semiconducting β-$FeSi_2$. β-$FeSi_2$ is known as a potential candidate for next-generation low-cost thin-film solar cells and has been widely studied for high-temperature thermoelectric applications.[24–28]

Despite containing abundant and low-cost constituent elements, the prolonged, multiple processing steps with vacuum requirements involved in synthesizing and stabilizing the phase increase the cost. This makes it important to develop a simple, low-cost method to synthesize β-$FeSi_2$. Dash *et al.* introduced molten salt shielded synthesis (MS^3 or MS3) to facilitate the synthesis of MAX phase Ti_3AlC_2, without requiring a vacuum or inert gas atmosphere.[29] In this method, the molten salt acts as a barrier to prevent oxidation at elevated temperatures. Furthermore, in the MXene literature, the synthesis of the MAX phase using different molten salts and tuning the properties has been widely studied. In this work, we demonstrate a molten salt shielded synthesis approach for the preparation of Mn-doped β-$FeSi_2$ powders under ambient air conditions using KBr encapsulation. In this work, KBr encapsulation is employed as a halide-based barrier to limit oxygen interaction during high-temperature processing. This approach suppresses oxidation and enables the synthesis of β-$FeSi_2$ under ambient conditions without the need for a vacuum or an inert atmosphere. This strategy provides a simpler and more scalable alternative to conventional molten salt and sodium flux methods. The optimized synthesis protocol enabled the formation of semiconducting Mn-doped β-$FeSi_2$ with minor Si and oxide secondary phases. This work aims to adopt the molten salt shielded synthesis method to produce oxidation-prone semiconducting materials in powder form under ambient air conditions.

2 Materials and methods

2.1 Synthesis

Elemental iron (Fe, ≥99.6%, Sigma-Aldrich), silicon (Si, ≥99.5%, Alfa Aesar, ∼325 mesh), and potassium bromide (KBr) powders were used as the starting materials. Manganese (Mn, ≥99.6%, Alfa Aesar) was added as a dopant. The nominal composition of the sample was $Fe_{1.99}Mn_{0.01}Si_5$. The required amounts of the powders were weighed and manually ground for 20 minutes using an agate mortar and pestle. The mixed powder was cold pressed into 10 mm pellets using a hydraulic press at 4 tons for 10 minutes. For encapsulation, a 13 mm die was first partially filled with KBr powder. The compacted pellet was placed at the center and completely covered with additional KBr to ensure full encapsulation. This assembly was then pressed again at 4 tons for 5 minutes; this process formed a protective KBr layer around the green pellet containing Fe, Si, and Mn. During heat treatment, this KBr layer acts as a physical barrier that limits direct exposure of the pellet to air.

The encapsulated pellet was positioned at the center of a salt bed in an alumina crucible and subjected to heat treatment under different temperature–time profiles, and each sample was named based on its heat-treatment conditions followed by the prefix "FS". The sample encapsulated and heat-treated at 1073 K for 24 h was named "FS-1073K/24h". The sample treated at 1273 K for 1 h followed by 1073 K for 4 h was named "FS-1273K/1h-1073K/4h". The sample treated at 1273 K for 15 minutes and then at 1073 K for 24 h was denoted as FS-1273K/15min-1073K/12h. After heat treatment, the samples were cooled to room temperature and washed with water to completely dissolve the KBr salt. The reacted compacted pellet was filtered. The dissolved salt solution was dried, and the recovered KBr salt was reused. A schematic of the synthesis process is shown in Fig. 1.

2.2 Characterization

The crystal structure and phase purity of the samples were examined using X-ray diffraction (XRD, Panalytical X'Pert3) with Cu Kα radiation (λ = 1.5406 Å). The XRD patterns were analyzed using Rietveld refinement in GSAS-II software to confirm phase purity and determine the lattice parameters of the prepared samples. The sample morphology was studied using a field-emission scanning electron microscope (FESEM, FEI Quanta 250 FEG). Elemental distribution was analyzed using EDS with an Oxford Instruments detector attached to the FEI Quanta 250 FEG. The density of Mn-doped β-$FeSi_2$ was measured using Archimedes' principle. Surface chemical composition and the electronic states of the elements were investigated using X-ray photoelectron spectroscopy (XPS, ULVAC-PHI VersaProbe 4, Japan) equipped with a monochromatic Al Kα source. The XPS data were analyzed using XPSPEAK41.

Room-temperature and temperature-dependent electrical resistivity were measured using a home-built four-probe

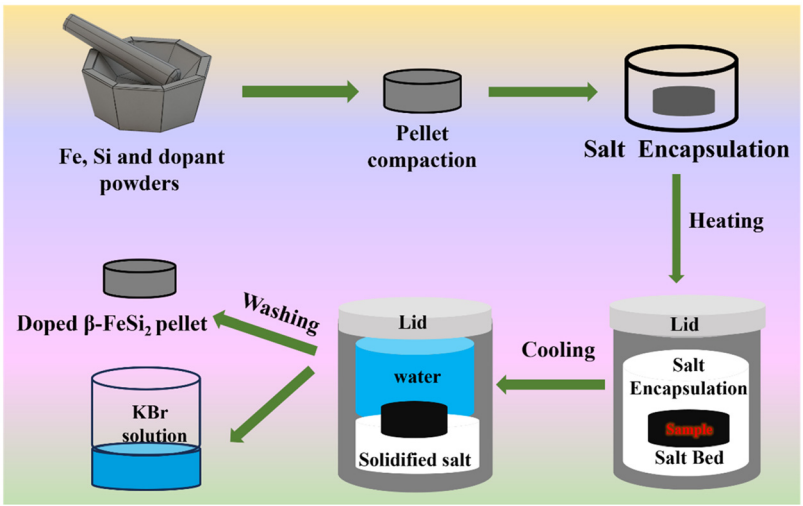

Fig. 1 Schematic of the steps involved in β-$FeSi_2$ synthesis.

apparatus based on the van der Pauw method. The room-temperature Seebeck coefficient was measured on the as-synthesized pellet using a home-built setup. In this setup, the sample was placed between two copper blocks, with one block heated using a micro-heater. The temperature difference between the blocks was monitored using a K-type thermocouple connected in differential mode. The voltage was measured using copper wires soldered onto the blocks, and the Seebeck coefficient was calculated as $\Delta V/\Delta T$ under steady-state conditions.

3 Results and discussion

Samples synthesized through the molten salt shielded synthesis method with different heating profiles were analyzed using X-ray diffraction, and the data are presented in Fig. 2a. The diffraction pattern labeled FS-1073K/24h corresponds to the encapsulated pellet heat-treated at 1073 K for 24 h. Detailed phase analysis shows the presence of Si, ε-FeSi, and α-Fe_2Si_5, indicating an incomplete reaction between the Fe and Si powders. To facilitate a faster eutectoid decomposition reaction to form β-$FeSi_2$, the encapsulated pellets were initially heat-treated at 1273 K for 15 minutes to 1 h. As per the phase diagram and earlier reports,[14] this treatment leads to the formation of α-Fe_2Si_5. These pellets were further heat-treated at 1073 K for different durations (4, 12, and 24 h). The XRD patterns of the pellets heat-treated at 1273 K for 15 minutes followed by 1073 K for 4, 12, and 24 h are shown in Fig. 2a. Phase analysis reveals mixed α- and ε-phases with minor silicon content for samples heat-treated for 4 and 12 h. However, the

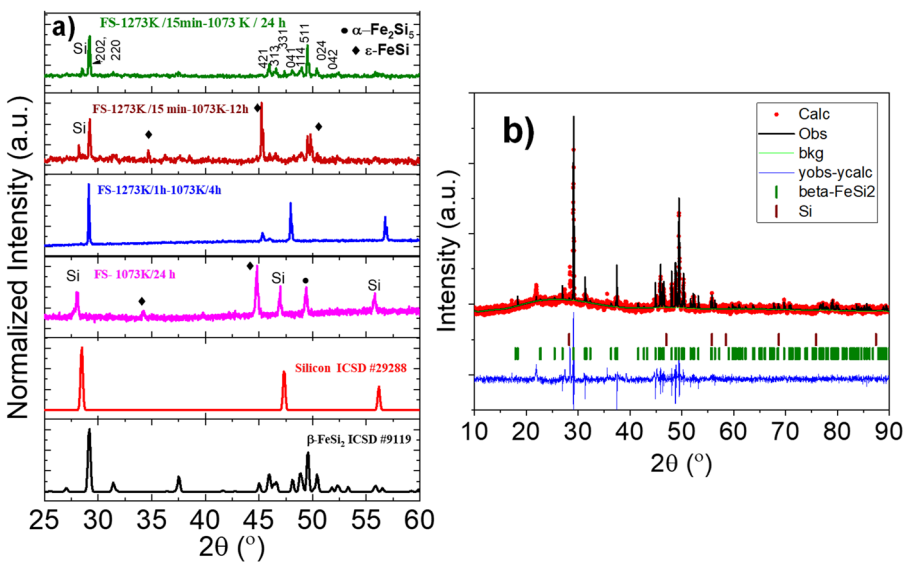

Fig. 2 (a) X-ray diffraction pattern of Mn-doped β-$FeSi_2$ samples synthesized under various heat treatment conditions. (b) Rietveld refinement of the sample FS-1273K/15min-1073K/24h.

Table 1 Lattice parameters and phase fractions of the encapsulated pellet FS-1273K/15min-1073K/24h

Sample	Density (g cm^{-3})	Phases present	wt%	Lattice parameters (Å)	GOF	wR
FS-1273/15min-1073K/24h	2.92	β-$FeSi_2$ Si	97.5 2.5	a = 9.8763(2), b = 7.7900(5), c = 7.8368 (4) a = 5.4291	1.43	3.16

pellet heat-treated at 1273 K for 15 minutes followed by 1073 K for 24 h shows peaks corresponding to β-$FeSi_2$ and Si only, indicating the formation of β-$FeSi_2$ with Si as a secondary phase.

Rietveld analysis of the diffraction pattern of the sample FS-1273K/15min-1073K/24h was carried out, and the results are shown in Fig. 2b. The refinement confirms that the pellet is X-ray pure and the phase fractions along with the calculated lattice parameters are given in Table 1. These results confirm that the two-step heat treatment is essential for achieving the formation of the β-$FeSi_2$ phase.

The refined lattice parameters agree well with the orthorhombic crystal structure of β-$FeSi_2$, matching the reference pattern (ICSD #9119). Silicon (Si) was detected as a secondary phase, which is expected from eutectoid decomposition. The intentional excess of Si promoted the formation of β-$FeSi_2$ while suppressing the formation of other iron-rich silicide phases.

Fig. 3a and b show the secondary electron micrographs of the sample heat-treated at 1273 K for 15 minutes followed by 1073 K for 24 h. The microstructure appears rough and porous, consisting of irregularly shaped particles. Some regions display partially sintered material, indicating incomplete densification resulting from the low-temperature eutectoid decomposition treatment. This porous morphology is anticipated to increase interfacial resistance, thereby affecting transport properties. Furthermore, elemental analysis of the sample surface was performed using energy dispersive spectroscopy (EDS), and the results are shown in Fig. 3c–f. The EDS mapping confirms a uniform distribution of Fe and Si, indicating good chemical homogeneity in the synthesized sample. The EDS spectrum shows major peaks for Fe and Si, with a low-intensity peak corresponding to Mn. The elemental mapping (Fig. 3d–f) shows the weight percentages of Fe and Si to be 52.9 wt% and 46.2 wt%, respectively. Elemental distribution mapping of Mn from EDS reveals a homogeneous dopant distribution. EDS mapping confirms the presence and uniform distribution of Mn and the absence of any nanoscale secondary phases. Also, no secondary Mn-containing phases were detected within the detection limit of XRD. Considering the low Mn concentration used in this study, which is well within the reported solubility limits in β-$FeSi_2$, Mn incorporation into β-$FeSi_2$ is possible.

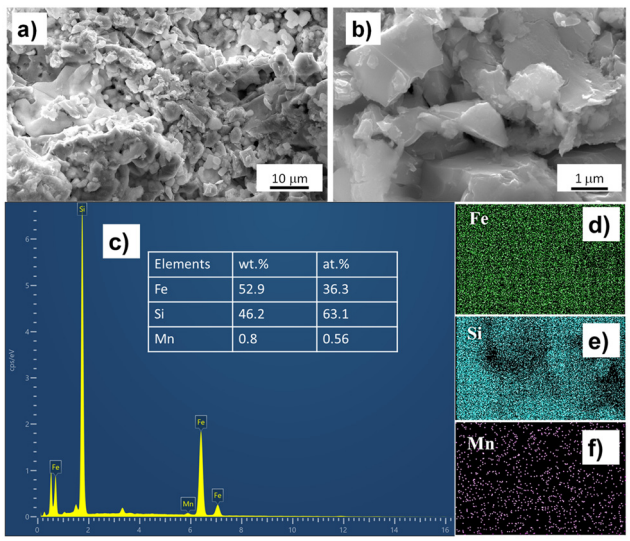

Fig. 3 Secondary electron micrographs of FS-1273K/15min-1073K/24h at (a) a 10 μm scale and (b) a 1 μm scale; (c) EDS spectrum; elemental mapping of (d) Fe, (e) Si and (f) Mn.

X-ray photoelectron spectroscopy (XPS) was performed to understand the chemical environment and oxidation states of the elements present on the sample surface. Fig. 4a shows the XPS survey spectrum of Mn-doped β-$FeSi_2$, which confirms the presence of elements Fe, Si and Mn. Fig. 4b shows the Fe 2p spectrum, in which the peaks at 707.5 eV and 720.2 eV are assigned to the spin–orbit doublet corresponding to Fe $2p_{3/2}$ and Fe $2p_{1/2}$ of the Fe–Si bond.[30,31] The area ratio between the peaks was 2 : 1 and the splitting energy was 12.7 eV. The peaks at 711–713 eV and 723–730 eV in the Fe 2p spectrum were deconvoluted into two peaks, which are associated with the oxidized Fe and satellite components, suggesting a possible surface oxide with a core silicide. The Si 2p spectrum (Fig. 4c) shows a broad peak between 101 and 103 eV, indicating the presence of Si in SiO_2, suggesting surface oxidation. The peak at 98.8 eV corresponds to the Si present in the $FeSi_2$ lattice and in elemental form. The O 1s peak at 531.2 eV indicates lattice oxygen arising from Fe–O and Si–O environments due to surface oxidation. The XPS peaks corresponding to oxidized species show the thin oxide layer formed on the surface of the material. The presence of a dominant Fe–Si peak at 102–103 eV and metallic components in the surface sensitive XPS spectra suggests the presence of the β-$FeSi_2$ phase with a native oxide layer. The Mn 2p spectrum (Fig. 4d) shows distinct spin–orbit splitting, with Mn $2p_{3/2}$ and Mn $2p_{1/2}$ peaks at 641.4 eV and 653.5 eV, respectively. The binding energies confirm the presence of Mn in the intermetallic or semiconducting matrix.

X-ray diffraction and X-ray photoelectron spectroscopy confirm the formation of the β-$FeSi_2$ phase with a minor Si secondary phase. Scanning electron microscopy and EDS analysis show a porous morphology with homogeneous elemental distribution, and the low density of the pellet (2.93 g cm^{-3}) is also verified using Archimedes' method, further confirming the porous nature of the sample. To investigate the semiconducting behavior of the synthesized pellets, temperature-dependent resistivity measurements were performed (Fig. 5). The resistivity is ~11 Ω cm at room temperature and decreases to ~0.82 Ω cm at 773 K. This reduction in resistivity with increasing temperature

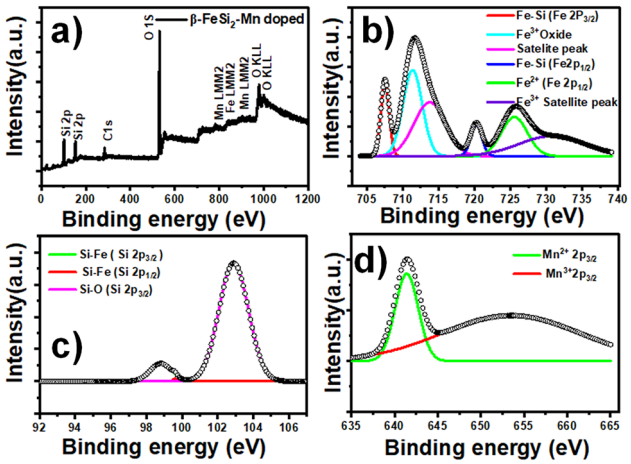

Fig. 4 X-ray photoelectron spectroscopy of the sample FS-1273K/15min-1073K/24h: (a) survey spectrum, (b) Fe 2p spectrum, (c) Si 2p spectrum and (d) Mn 2p spectrum.

confirms the semiconducting nature of the β-$FeSi_2$ sample. The resistivity of β-$FeSi_2$ reported in the literature typically varies between $\sim 10^{-2}$ and 1 Ω cm. The present sample exhibits significantly higher resistivity. This is attributed to the low density and porous microstructure, which leads to poor inter-particle electrical contact, increased grain boundary scattering and minor additional contribution from the surface oxides. The measured transport properties are dominated by extrinsic microstructural effects rather than intrinsic behavior.[11,12,30]

The temperature-dependent resistivity data were further used to plot $1000/T$ *versus* $\ln \rho$, from which the activation energy was estimated to be ~0.63 eV from the slope of the intrinsic region. Considering the reported intrinsic band gap of β-$FeSi_2$ (~0.8–0.9 eV), the lower activation energy can be attributed to Mn-induced impurity states and grain boundary effects arising from the porous microstructure. Therefore, the extracted value represents an effective activation energy. The room-temperature

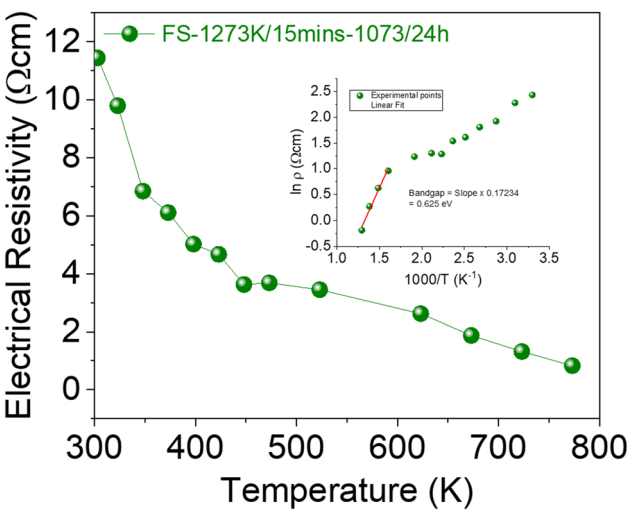

Fig. 5 Temperature-dependent electrical resistivity of the sample FS-1273K/15min-1073K/24h (inset showing a plot of $1000/T$ *vs.* $\ln \rho$).

Seebeck coefficient (S) of the as-synthesized pellet, measured using a home-built apparatus, is $+102 \pm 4$ μV K^{-1} for the sample FS-1273K/15min-1073K/24h. The positive Seebeck coefficient confirms that the sample is p-type. The power factor, calculated using the equation $PF = S^2/\rho$, is 0.095 μW m^{-1} K^{-2}. These values are lower than those reported in the literature for β-$FeSi_2$, which can be attributed to the low density of the synthesized pellets. The presence of the Si secondary phase, which is a semiconductor with relatively high electrical resistivity compared to β-$FeSi_2$ could suppress electrical conduction. However, at this low concentration, it is expected to be present as a secondary dispersed phase rather than forming a continuous network. Therefore, its contribution is likely limited to a minor increase in overall resistivity and possible grain boundary scattering effects, without dominating the transport behavior. The temperature-dependent resistivity trend and room-temperature resistivity observed suggest that bulk β-$FeSi_2$ conduction remains the primary transport mechanism. Although the thermoelectric properties are modest, this method is effective for synthesizing β-$FeSi_2$ powder, which can be useful for composite thermoelectric and photovoltaic applications.

4 Conclusions

In this work, semiconducting Mn-doped β-$FeSi_2$ has been successfully synthesized using the molten salt shielded synthesis method in ambient air. The phase composition and morphology of the synthesized sample were analyzed using XRD, SEM and EDS. The temperature-dependent electrical resistivity confirms the presence of the semiconducting phase. This method provides a simple and scalable synthesis route under ambient air conditions without the need for a vacuum or an inert atmosphere. Overall, this study demonstrates a viable synthesis route that can be extended to large-scale synthesis of doped silicides for energy applications. Furthermore, this method can be adopted to synthesize other oxidation-prone semiconducting materials in powder form under ambient atmospheric conditions. Conventional methods rely on vacuum-assisted processes such as arc melting combined with hot pressing and prolonged heat treatment, which significantly increase manufacturing cost and limit scalability. In this work, we demonstrate a vacuum-free powder manufacturing route for silicides using simple furnace processing. Although the thermoelectric performance is limited by low density, the synthesized powders can be used for scalable composite/flexible thermoelectric and photovoltaic hybrid devices.

Author contributions

Hemalatha M Sivaprakasam: conceptualization, investigation, methodology and writing – original draft. Rajasekar Parasuraman: conceptualization, supervision, validation and writing – review & editing. Arun Anand Prabhu: supervision, project administration and formal analysis.

Conflicts of interest

There are no conflicts to declare.

Data availability

The data that support the findings of this study are available from the corresponding authors upon reasonable request.

Acknowledgements

The authors would like to acknowledge the VIT management and sponsored research office for infrastructural facilities and financial support in the form of a seed grant. The authors gratefully acknowledge the Instrumentation Facility at Vellore Institute of Technology, Vellore, India, for providing access to X-ray diffraction (XRD), X-ray photoelectron spectroscopy (XPS), and field emission scanning electron microscopy (FE-SEM) facilities. The authors would also like to thank Dr. Sathishkumar Palaniyappan for his timely assistance with the XRD measurements and data acquisition.

References

1 X. Chen and C. Liang, *Catal. Sci. Technol.*, 2019, **9**, 4785–4820.
2 P. Sangwan and S. Muthiah, *J. Mater. Sci.: Mater. Electron.*, 2023, **34**, 1879.
3 J.-i Tani and H. Kido, *Jpn. J. Appl. Phys.*, 2000, **39**, 1054.
4 U. Birkholz and J. Schelm, *Phys. Status Solidi B*, 1968, **27**, 413–425.
5 J. Cheng, L. Gan, J. Zhang, J. Xi, L. Xi, J. Yang, T. Deng, P. Qiu, X. Shi and L. Chen, *J. Mater. Sci. Technol.*, 2024, **187**, 248–257.
6 K. Lefki, P. Muret, N. Cherief and R. Cinti, *J. Appl. Phys.*, 1991, **69**, 352–357.
7 S. Sam, K. Yamazaki and H. Nakatsugawa, *Mater. Proc.*, 2026, **26**, 7.
8 K. H. Tan, K. L. Pey and D. Z. Chi, *J. Appl. Phys.*, 2009, **106**(2), 023712.
9 M. Ito, H. Nagai, E. Oda, S. Katsuyama and K. Majima, *J. Appl. Phys.*, 2002, **91**, 2138–2142.
10 L. Abbassi, D. Mesguich, L. Coulomb, G. Chevallier, R. Aries, C. Estournès, E. Flahaut, R. Viennois and M. Beaudhuin, *J. Alloys Compd.*, 2022, **902**, 163683.
11 S. Sam, S. Say, K. Yamazaki and H. Nakatsugawa, *Sci. Technol. Adv. Mater.*, 2025, **26**, 2585555.
12 M. Zhu, X. Wang, Y. Yan, S. Chen, W. Zhang, H. Kang, E. Guo, Z. Chen, R. Chen and T. Wang, *ACS Appl. Mater. Interfaces*, 2026, **18**(11), 16707–16715.
13 H. Alqurashi, *Int. Commun. Heat Mass Transfer*, 2026, **175**, 111244.
14 I. Yamauchi, S. Ueyama and I. Ohnaka, *Mater. Sci. Eng., A*, 1996, **208**, 108–115.
15 P. E. Turchi, V. I. Ivashchenko, V. Shevchenko, L. Gorb, J. Leszczynski and A. Perron, *Appl. Sci.*, 2023, **13**, 12669.
16 I. Yamauchi, T. Okamoto, H. Ohata and I. Ohnaka, *J. Alloys Compd.*, 1997, **260**, 162–171.
17 K. Han, M. Saito, J. Xia, I. Ohnuma and R. Kainuma, *J. Alloys Compd.*, 2022, **919**, 165810.
18 U. Ail, S. Gorsse, S. Perumal, M. Prakasam, A. Umarji, S. Vivès, P. Bellanger and R. Decourt, *J. Mater. Sci.*, 2015, **50**, 6713–6718.
19 P. Rajasekar and A. M. Umarji, *Intermetallics*, 2017, **89**, 57–64.
20 F. L. B. M. Redzuan, I. Mikio and T. Masatoshi, *J. Mater. Sci.*, 2018, **53**, 7683–7690.
21 S.-C. Ur, I.-H. Kim and J.-I. Lee, *Met. Mater. Int.*, 2002, **8**, 169–175.
22 T. Yamada and H. Yamane, *Chem. Mater.*, 2007, **19**, 6047–6051.
23 T. Yamada, H. Morito and H. Yamane, *Jpn. J. Appl. Phys.*, 2009, **48**, 100209.
24 L. Abbassi, D. Mesguich, L. Coulomb, G. Chevallier, R. Aries, C. Estournès, E. Flahaut, R. Viennois and M. Beaudhuin, *J. Alloys Compd.*, 2022, **902**, 163683.
25 W. Shen, S. Shen, W. Tang and L. Wang, *Narrow Gap Semiconductors 1995*, CRC Press, 2020, pp. 90–94.
26 K. Lefki, P. Muret, N. Cherief and R. Cinti, *J. Appl. Phys.*, 1991, **69**, 352–357.
27 S. Muthiah, *et al.*, *Ceram. Int.*, 2022, **48**, 29366–29371.
28 P. Sangwan, N. K. Upadhyay, R. Shyam, P. Gupta, H. Kumar, S. Singh, A. Pandey and S. Muthiah, *Hybrid Adv.*, 2025, **9**, 100423.
29 A. Dash, R. Vaßen, O. Guillon and J. Gonzalez-Julian, *Nat. Mater.*, 2019, **18**, 465–470.
30 F. Esaka, H. Yamamoto, H. Udono, N. Matsubayashi, K. Yamaguchi, S. Shamoto, M. Magara and T. Kimura, *Appl. Surf. Sci.*, 2011, **257**, 2950–2954.
31 S. Sen, P. Guha, P. Banerji and P. Pramanik, *RSC Adv.*, 2016, **6**, 68238–68246.